

Controlled Growth of 1D MoSe₂ Nanoribbons with Spatially Modulated Edge States

Fang Cheng,^{†,§} Hai Xu,^{†,§} Wentao Xu,^{‡,§} Pinjia Zhou,^{‡,§} Jens Martin,^{*,‡,§} and Kian Ping Loh^{*,†,§}

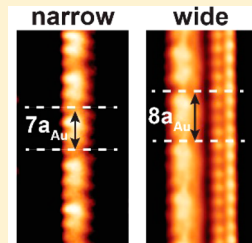
[†]Department of Chemistry, National University of Singapore, Singapore 117543

[‡]Department of Physics, National University of Singapore, Singapore 117551

[§]Centre for Advanced 2D Materials and Graphene Research Centre, National University of Singapore, Singapore 117546

Supporting Information

ABSTRACT: Two-dimensional (2D) transition metal dichalcogenides (TMDCs) possess interesting one-dimensional (1D) properties at its edges and inversion domain boundaries, where properties markedly different from the 2D basal plane, such as 1D metallicity and charge density waves, can be observed. Although 2D TMDCs crystals are widely grown by chemical vapor deposition (CVD), the fabrication of 1D TMDCs ribbons is challenging due to the difficulty to confine growth in only one dimension. Here we report the controlled growth of MoSe₂ nanoribbons with an aspect ratio >100 by using prepatterned Se reconstructions on Au(100). Using scanning tunneling microscope and spectroscopy (STM/STS), the atomic and electronic structure of MoSe₂ nanoribbons are studied. The ultranarrow ribbons show metallic behavior, while wider ribbons show a crossover from metallic to semiconducting behavior going from the edge to the center of the ribbon. The observed conductance modulations of the ultranarrow ribbons are attributed to 1D Moiré pattern. Remarkably, it shows a different periodicity compared with the 2D Moiré pattern in wider ribbons indicating that the 1D system is softened due to the high ratio of edge to basal plane bonds. Further, we demonstrated that the nanoribbons are stable against ambient conditions, which suggests that 1D TMDCs can be exploited for further applications.



KEYWORDS: Transition metal dichalcogenides, nanoribbon, molecular beam epitaxy, Moiré pattern, scanning tunneling microscopy, edge state

Dimensional engineering of three-dimensional (3D) crystals to create two-dimensional (2D) and one-dimensional (1D) structures leads to the rearrangement of the atomic lattice and appearance of new properties. 2D transition metal dichalcogenides (TMDCs) have attracted great interest beyond graphene because of their thickness-dependent energy gaps and large spin-orbit coupling, which promise applications in transistors and optically controllable spintronics.^{1–6} Interesting 1D characteristics have emerged at regions of 2D discontinuity, for example, at the edges and domain boundaries of 2D crystals.⁷ 1D metallicity has been proposed to occur universally at the edges or domain boundaries of TMDC, due to the polar discontinuity at its interfaces, where free carriers accumulate to quench the localized charges.⁸ However, the charge density wave (CDW) order has been recently observed at the twin mirror boundaries of MoSe₂ leading to the opening of a small band gap in 1D dispersion.⁷ Furthermore, it is well-known that the semiconducting 2H phase of MoS₂ doped to increase its electron density rearranges the atomic lattice from the original trigonal prismatic (2H) to octahedral form (1T).^{9–13} The metallic 1T phase is unstable against Peierls distortion and reconstructs into 1D zigzag chains (1T' phase) with a small energy gap opening.¹⁴

To investigate the intrinsic physical properties of the 1D TMDC nanoribbon and its edge structure, it is necessary to isolate the 1D nanoribbon from the 2D bulk. A recent

transmission electron microscopy study reveals that MoSe₂ nanowires are unstable when it is downsized to the narrowest possible free-standing wire. Instead, a phase transition from MoSe₂ to MoSe was observed, along with variations in conductance from semiconducting to metallic behavior.¹⁵ It is important to note that these nanowires were sculptured from the 2D counterpart by a highly energetic electron beam, which could have induced the phase transition. In contrast to top-down cutting or lithographic methods, bottom-up growth on surfaces with broken symmetry may stabilize the formation of 1D nanowires. Herein, Au (100) is chosen as the substrate due to its anisotropic reconstructions. Surface atoms of Au (100) are reconstructed into a layer of quasi-hexagonal structure, consisting of close-packed rows of Au atoms arranged along two high symmetric ⟨110⟩ directions.^{16–19} The adsorption of chalcogen atoms is expected to redistribute gold atoms within the hexagonal layers leading to new reconstructions.

Previously, 2D MoSe₂ has been coupled to gold plasmonic nanostructures as it has a smaller band gap and higher electron mobility than MoS₂.²⁰ Herein, we examined the growth of 1D MoSe₂ nanoribbon on selenium-enriched Au (100) surface using molecular beam epitaxy techniques. Using high-resolution

Received: November 10, 2016

Revised: January 3, 2017

Published: January 16, 2017



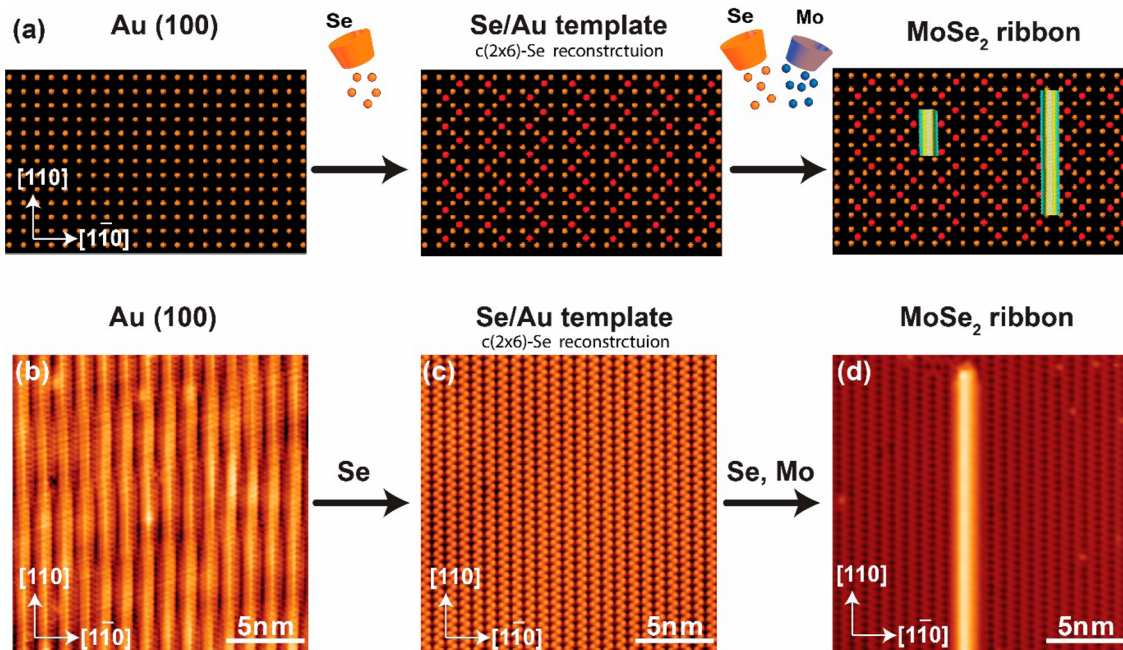


Figure 1. Two-step controlled growth of MoSe₂ ultranarrow ribbon on Au(100). (a) Schematic illustration of growth method. (b–d) Typical STM images of clean Au(100) surface (b), c(2 × 6)-Se/Au reconstruction template (c), and MoSe₂ ultranarrow ribbon on template (d). $V = -1.0$ V, $I = 0.2$ nA.

scanning tunnelling microscopy (STM), we further resolved the edge structure of MoSe₂ nanoribbon and studied its distortion when the ribbon was reduced to the narrowest possible repeating unit. A change in the electronic structure of the ribbon during dimensional crossover from 2D to 1D was also identified.

For the fabrication of MoSe₂ nanoribbons, we employed a two-step growth method (Figure 1). First, Se atoms were evaporated onto Au(100) to form a preassembled Se/Au template. Second, Mo and Se were codosed onto the template surface to form MoSe₂ nanoribbons. Figure 1b shows a typical STM image of clean Au(100). Distinct from unreconstructed Au(100)-(1 × 1) structure, the surface shows the Au(100)-(5 × 23) reconstruction.^{16–19} The adsorption of selenium atoms onto this surface results in a change to form distinct Au–Se reconstructions. Different reconstructions, specifically p(2 × 2)-Se, c(2 × 6)-Se, and a mixed phase were obtained by tuning the selenium coverage on Au(100). The detailed growth conditions and STM images can be found in Supporting Information part 1 and Figure S1. By using the c(2 × 6)-Se template surface, we identify a growth regime which allows for ultranarrow ribbons to grow with large aspect ratios.

Starting from the c(2 × 6)-Se reconstruction, Mo and Se atoms were deposited simultaneously onto the preassembled Au–Se template using a flux ratio of ~1:2. Remarkably, we observed ultranarrow ribbons growing along the $\langle 110 \rangle$ directions, and the ribbon width is confined between two zigzag Se-chains. The close-up STM images and line profiles in Figure S2 reveal the exact location of ultranarrow ribbon with respect to the Au–Se template. The ribbon is confined between two Se zigzag chains, while the center of the ribbon is overlapping with a Se zigzag chain in the middle. Since the c(2 × 6)-Se template is an anisotropic surface, the diffusion energy of atoms along the zigzag chain can be expected to be much lower than that across the chain, which explains how 1D growth of MoSe₂ ultranarrow ribbons can be obtained on this surface.

By increasing the dose time of Mo and Se atoms, the ultranarrow ribbons grow to as long as the size of the underlying Au(100) terrace without becoming wider (Figure S3).

By tuning the growth parameters, wider ribbons with width >2 nm can be grown on Au(100). In this case, instead of the codeposition of Mo and Se atoms, only Mo atoms were deposited onto c(2 × 6)-Se template surface. The typical surface morphology, the wetting layer structure, and the statistical analysis of ribbon widths are shown in Figure S4. The ribbons shown in Figure S4a are much wider and shorter compared with ultranarrow ribbons. The width distribution, as judged by analyzing several large-scale STM images, is highly heterogeneous. The STM image of the wetting layer exhibits a mixed phase (Figure S4b), which resembles the structure shown in Figure S1c. When Mo atoms are deposited onto c(2 × 6)-Se template surface without Se, they consume available Se atoms on the template surface to form MoSe₂. As the coverage of Se atoms decreases, the wetting layer structure changes from the original c(2 × 6)-Se to a mixed phase (Figure S4b), which is consistent with our coverage dependent study shown in Figure S1. Since the distance between zigzag chains is variable in the mixed phase, it causes a wide variation in the widths of the grown ribbon.

To elucidate the atomic structure of the ultranarrow ribbon, we acquired high-resolution STM images of the ribbon. As shown in Figure 2a, the ribbon can be resolved as three atomic chains with hexagonal arrangement, where the position of Se atoms is indicated by black circles. Line profiles reveal that the width of the ribbon is ~6.90 Å and the average lattice along the axis of the ribbon is ~3.36 Å. Based on the observation of three atomic chains and the hexagonal structure in STM image, we propose that the ultranarrow ribbon is composed of only one hexagonal unit with Se termination to saturate the dangling bond of the Mo-edge, which in fact constitutes the narrowest possible ribbon. Figure 2c shows the structure model of the

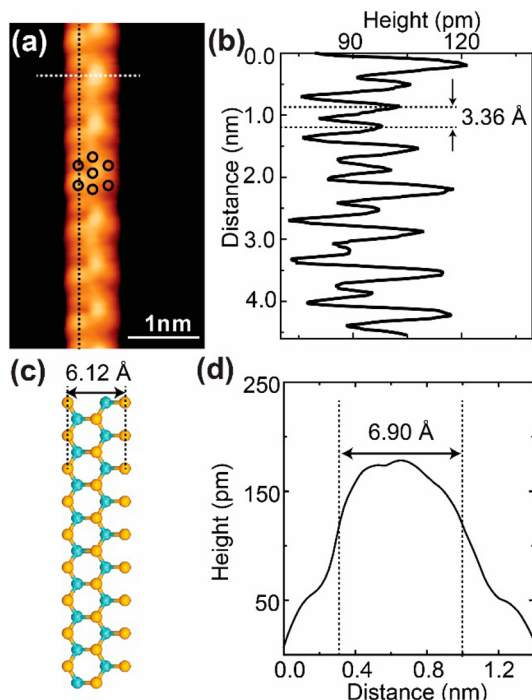


Figure 2. Atomic structure of MoSe₂ ultranarrow ribbon on Au(100). (a) High-resolution STM image of MoSe₂ ultranarrow ribbon. The position of Se atoms are labeled as black circles ($V = -10$ mV, $I = 1.0$ nA). (b, d) Line profile obtained along (b) and across (d) ultranarrow ribbon. (c) The structure model of ultranarrow ribbon.

ulnanarrow ribbon. In this model, the width of the ribbon is 6.12 Å from the positions of Se atoms at two edges, which is consistent with the measured 6.90 Å.

To gain insights into the electronic structure of the ulnanarrow ribbon, STS measurements were performed on the ribbon. Shown in Figure 3e is a typical spectrum recorded

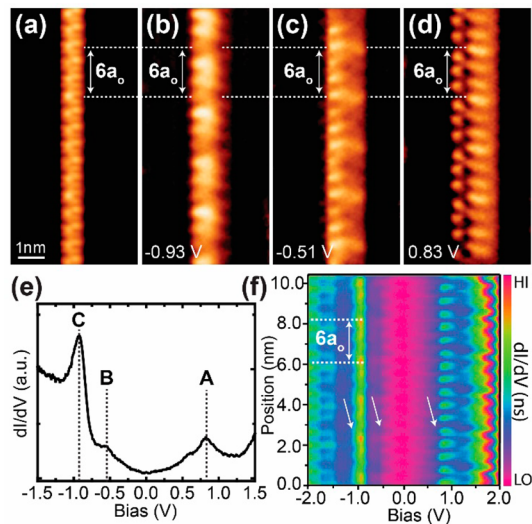


Figure 3. Electronic structure of MoSe₂ ultranarrow ribbon. (a) STM topological image ($V = -20$ mV, $I = 1.0$ nA). (b-d) STS maps at fixed bias: -0.93 V (b), -0.51 V (c), and 0.83 V (d). (e) STS spectra obtained on ultranarrow ribbon. (f) 2D plot of various dI/dV line scans measured along the ultranarrow ribbon with a distance step of 0.5 Å. The superlattice of 6L are indicated.

at the center of the ribbon, which reveals metallic characteristics, distinct from the intrinsic semiconducting behavior of 2D MoSe₂ island. Moreover, the STS data on the ulnanarrow ribbon show three notable states. The state A, located at ~ 0.83 V, is assigned to the onset of the MoSe₂ conducting band, which is analogous to what was reported on 2D MoS₂ islands.²¹ The states B (-0.51 V) and C (-0.93 V) in the negative bias regime are characteristic states of 1D MoX₂ (X = S or Se) structure. A similar peak as B has been found on MoSe₂ boundary on HOPG,²² and a similar peak as C was reported on the MoS₂ wire.²³ To investigate the spatial distribution of these states in the ulnanarrow ribbons, STS maps were taken at bias voltage of -0.93 V (Figure 3b), -0.51 V (Figure 3c), and 0.83 V (Figure 3d). Clearly, the local conductance fluctuates periodically along the ribbon at all of these three bias voltages. The average period of the oscillation is 2.01 ± 0.08 nm, which is approximately 6 times of the lattice constant of ulnanarrow ribbon ($L = 3.36$ Å). The 6L super structure is also verified by the sequentially acquired atomic resolution STM images (Figure 3a) which have no noticeable thermal drift. To further investigate spatial distribution of LDOS, detailed dI/dV line scans were performed along the ribbon with a fine step of 0.5 Å. The space and energy resolved two-dimensional conductance map along the ribbon is shown in Figure 3f. The super structure of 6L can be clearly observed for states A to C (marked by white arrows).

We performed a comparative study on the topological and electronic structure of the wide ribbon. Figure 4 shows an STM

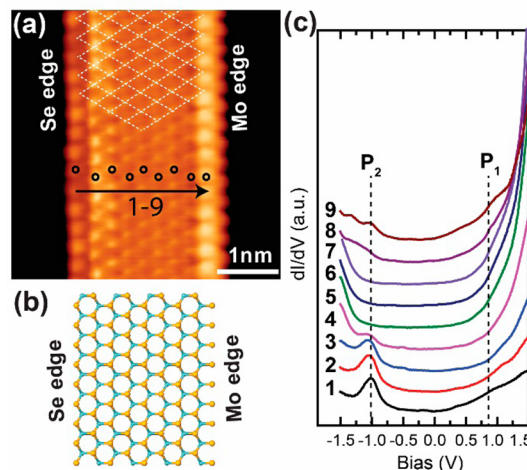


Figure 4. Topological and electronic structure of a wide MoSe₂ ribbon. (a) Atomic resolution STM image of a wide ribbon (width ~ 2.5 nm) ($V = -100$ mV, $I = 1.0$ nA). (b) Structure model of the wide ribbon. The left edge is the Se-edge, and the right edge is Se-terminated Mo-edge. (c) Position-dependent STS spectra acquired on different Se atoms across the ribbon. Numbers 1–9 indicate the position of the tip where the spectra are acquired.

image and position-dependent STS spectra on a wide ribbon. The atomic-resolution STM image reveals a hexagonal lattice with an average lattice constant of ~ 3.26 Å, which is close to value of the bulk counterpart (3.29 Å). The grid superimposed on Figure 4a indicates the atoms at the right edge have half of a lattice displacement compared with atoms in the basal plane. Based on a previous study of 2D MoS₂ islands,^{24,25} the right edge is the Se-terminated Mo-edge, and the left edge should be the Se-edge (Figure 4b). Shown in Figure 4c are STS spectra

acquired on different Se atoms across the ribbon width. To quantitatively compare the spectra, all of the spectra were acquired under the same conditions. Before the feedback loop was interrupted, the tip was fixed at the same height above the surface using the same tunneling conditions ($V = -2.0$ V, $I = 1.0$ nA). Moreover, the same bias modulation (987 Hz, 10 mV) was used during spectra collection. To avoid thermal drift, the STM image of the wide ribbon was recollected after recording each spectrum, and the tip was positioned on each Se atom based on the newly collected STM image. The spectra were displaced in y -axis for comparison. Two notable features (P_1 and P_2) are observed in spectra acquired close to the two edges. P_1 is located at ~ 0.80 V, similar to state A, and can be assigned to the onset of MoSe_2 conducting band. P_2 (~ -1.00 V) is close to state C, and we assign it as the Se-dominated edge state as its intensity is strongest at the edges. To double check, a series of spectra were acquired across a ribbon starting from the Au–Se wetting layer (Figure S5). STS on the Au–Se surface show no obvious peak confirming that P_1 and P_2 originate from MoSe_2 edges. When the tip moves toward the center of the ribbon only a few atomic distances away from the edges, a very flat feature is detected in the bias range of -1.2 to 0.5 V (STS spectra S5–7). The original dI/dV curves without y -axis displacement are shown in linear and logarithmic scale in Figure S6 demonstrating the conductivity of the center is indeed much lower than that of the edge. Judging from $\log(dI/dV) - V$, the edges of wide ribbon show a metallic behavior, which is consistent with the metallic edges observed on triangular MoS_2 islands.²⁶ Although STS show nonzero local density of states (LDOS) in the center of ribbon, our observations resemble spectra with a semiconducting gap and additional direct tunneling to Au donor states.²¹ Therefore, the STS recorded on the wide ribbon confirms the presence of localized states at the edges of the ribbons, which are absent at the center of the ribbon.

Previously, conductance modulations in 1D metallic modes at inversion domain boundaries of MoSe_2 have been rationalized on the basis of standing waves due to Bragg reflection of the superlattice potential, as well as quantum well states due to the finite length of defects at these boundaries.²² In this case, however, the periodicity of modulation is the same at different energies in contradiction to energy-dependent wavelengths in quantum well states. Further, the CDW order has been used to explain the conductance modulation observed in mirror twin boundaries of MoSe_2 on bilayer graphene.⁷ We rule out CDW because no energy gap is observed around the Fermi level. In fact, the close correlation between topographical and conductance modulations on the surface suggest that the conductance modulation is related to the 1D Moiré pattern arising from the lattice commensuration between 1D MoSe_2 and the gold substrate. In order to verify this, STS maps were conducted on the wide ribbons as well. Shown in Figure 5a and b are two STS maps of ultranarrow and wide ribbon. The line profiles reveal the different periodicities of the conductance modulations in both ribbons. The periodicity is 2.01 nm in ultranarrow and 2.30 nm in the wide ribbon, respectively. According to the formula for the Moiré pattern [$a_{\text{MoSe}_2}a_{\text{Au}}/(a_{\text{MoSe}_2} - a_{\text{Au}})$], the period of the Moiré pattern is 2.00 nm for ultranarrow ribbon ($a_{\text{MoSe}_2} = 3.36$ Å, $a_{\text{Au}} = 2.88$ Å) and 2.36 nm for wide ribbon ($a_{\text{MoSe}_2} = 3.26$ Å). These values are close to our measurement values. As illustrated in Figure 5d, one period of the Moiré pattern is due to the interference pattern between $6a_{\text{MoSe}_2}$ of the ultranarrow ribbon with the underlying $7a_{\text{Au}}$

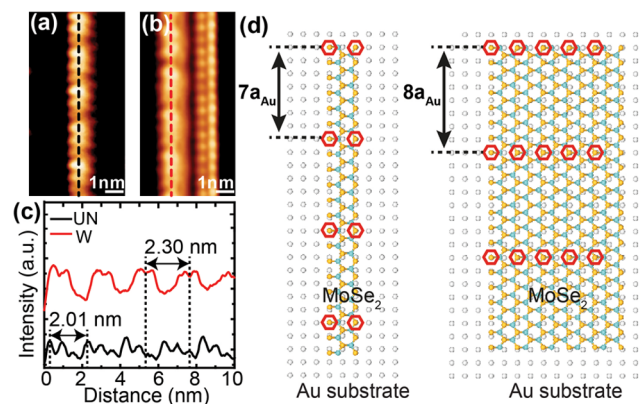


Figure 5. Comparative study of conductance modulation in MoSe_2 ultranarrow ribbon and wide ribbon. (a–b) STS maps on an ultranarrow ribbon ($V = -0.93$ V, $I = 1.0$ nA) and wide ribbon ($V = -1.0$ V, $I = 1.0$ nA). (c) The line profile acquired along the dash lines shown in parts a and b. “UN” represents ultranarrow ribbon, and “W” represents wide ribbon. (d) A model illustrates lattice-distortion induced conductance modulation in ultranarrow ribbon and wide ribbon.

lattice of Au(100), while it appears when $7a_{\text{MoSe}_2}$ of wide ribbon coincides with the underline $8a_{\text{Au}}$ of Au(100).

We argue that the distinct Moiré pattern for ultranarrow 1D ribbons is due to softening of the ribbons. When the ribbon structure is narrowed down to 1D, the ratio of edge bonds to intraplane bonds increases significantly, and ultimately the elastic and electronic properties of the 1D structure will be dominated by edges. Consequently, we may expect variation in Moiré pattern. Previously, a 1D Moiré pattern was observed in doubled-walled carbon nanotube displaying a strong modification of electronic properties in the material.^{27–29} The different Moiré patterns in the ultranarrow ribbon compared to wide ribbon and 2D bulk demonstrates that the lattice in ultranarrow ribbon is distorted. Apparently, the increased influence of edges softens the ribbon and making it more pliable. We speculate that introduction of tensile strain in the ribbon may be beneficial to minimize Coulomb repulsion due to charge accumulation along the edge indicated by DFT calculations.³⁰ Another possibility is that the interaction between Se-terminated edge and Au-substrate favors a $6a_{\text{MoSe}_2}$ Moiré pattern. Certainly, the dominant role of edges after Moiré pattern is supported by the observation of the metallic behavior.

In order to evaluate the potential for further applications of as-grown MoSe_2 nanoribbons, samples were exposed to air for 1 h and then transferred back into the ultrahigh vacuum (UHV) chamber and checked by STM again (Figure S7). Although the Se wetting layer becomes blurred (Figure S7b), possibly due to water or gas adsorption, the atomic structure of MoSe_2 ribbons is still observable (inset of Figure S7b) indicating that ribbons are stable in air. Simply by outgassing the sample in UHV chamber at ~ 200 °C for 15 min, the Se wetting layer is recovered, and clear STM image of MoSe_2 ribbons can be obtained (Figure S7c).

In conclusion, by employing preassembled Se-reconstruction on Au(100) we have successfully fabricated ultranarrow ribbons (~ 0.7 nm) with high aspect ratio greater than 100. The ultranarrow ribbon are grown on the c(2 × 6)-Se template surface when codepositing Mo and Se with a flux ratio $\sim 1:2$. The ultranarrow ribbon is metallic as measured using STS.

Wide ribbon (>2 nm) displays metallic edges and semiconducting center. The spatial conductance oscillations of the edge states along the length of the ultranarrow ribbon is induced by a 1D Moiré pattern formed by commensurate interactions between 1D MoSe₂ ribbon and Au (100) substrate. The periodicity of 1D Moiré pattern in ultranarrow ribbon is different from that of the 2D Moiré pattern in wider ribbons, indicating that the 1D system is soft due to the higher weight of edge to basal plane atomic bonding. The nanoribbons show good air stability, suggesting technological exploitations may be possible if fabrication process can be scaled up.

■ ASSOCIATED CONTENT

Supporting Information

The Supporting Information is available free of charge on the ACS Publications website at DOI: [10.1021/acs.nanolett.6b04715](https://doi.org/10.1021/acs.nanolett.6b04715).

Details of the experiment method, additional STM images of Se–Au reconstructions, and STM/STS of ultranarrow and wide ribbons ([PDF](#))

■ AUTHOR INFORMATION

Corresponding Authors

*E-mail and phone number: phyjm@nus.edu.sg, 65-65164140.
*E-mail and phone number: chmlohkp@nus.edu.sg, 65-65164402.

ORCID®

Fang Cheng: [0000-0003-1645-4237](https://orcid.org/0000-0003-1645-4237)

Kian Ping Loh: [0000-0002-1491-743X](https://orcid.org/0000-0002-1491-743X)

Notes

The authors declare no competing financial interest.

■ ACKNOWLEDGMENTS

The authors thank funding and infrastructure support by the Singapore-Berkeley Research Initiative for Sustainable Energy (SinBeRISE), and National Research Foundation (NRF), Singapore, Midsized Centre grant (CA2DM) under the Prime Minister's Office.

■ REFERENCES

- (1) Mak, K. F.; McGill, K. L.; Park, J.; McEuen, P. L. *Science* **2014**, *344*, 1489–1492.
- (2) Wang, Q. H.; Kalantar-Zadeh, K.; Kis, A.; Coleman, J. N.; Strano, M. S. *Nat. Nanotechnol.* **2012**, *7*, 699–712.
- (3) Lv, R.; Robinson, J. A.; Schaak, R. E.; Sun, D.; Sun, Y.; Malloouk, T. E.; Terrones, M. *Acc. Chem. Res.* **2015**, *48*, 56–64.
- (4) Zeng, H.; Dai, J.; Yao, W.; Xiao, D.; Cui, X. *Nat. Nanotechnol.* **2012**, *7*, 490–493.
- (5) Cao, T.; Wang, G.; Han, W.; Ye, H.; Zhu, C.; Shi, J.; Niu, Q.; Tan, P.; Wang, E.; Liu, B.; Feng, J. *Nat. Commun.* **2012**, *3*, 887.
- (6) Radisavljevic, B.; Radenovic, A.; Brivio, J.; Giacometti, V.; Kis, A. *Nat. Nanotechnol.* **2011**, *6*, 147–150.
- (7) Barja, S.; Wickenburg, S.; Liu, Z.-F.; Zhang, Y.; Ryu, H.; Ugeda, M. M.; Hussain, Z.; Shen, Z.-X.; Mo, S.-K.; Wong, E.; Salmeron, M. B.; Wang, F.; Crommie, M. F.; Ogletree, D. F.; Neaton, J. B.; Weber-Bargioni, A. *Nat. Phys.* **2016**, *12*, 751–756.
- (8) Gibertini, M.; Marzari, N. *Nano Lett.* **2015**, *15*, 6229–6238.
- (9) Cheng, Y.; Nie, A.; Zhang, Q.; Gan, L.-Y.; Shahbazian-Yassar, R.; Schwingenschlogl, U. *ACS Nano* **2014**, *8*, 11447–11453.
- (10) Voiry, D.; Goswami, A.; Kappera, R.; Silva, C.; Kaplan, D.; Fujita, T.; Chen, M.; Asefa, T.; Chhowalla, M. *Nat. Chem.* **2014**, *7*, 45–49.
- (11) Acerce, M.; Voiry, D.; Chhowalla, M. *Nat. Nanotechnol.* **2015**, *10*, 313–318.
- (12) Kappera, R.; Voiry, D.; Yalcin, S. E.; Branch, B.; Gupta, G.; Mohite, A. D.; Chhowalla, M. *Nat. Mater.* **2014**, *13*, 1128–1134.
- (13) Enyashin, A. N.; Yadgarov, L.; Houben, L.; Popov, I.; Weidenbach, M.; Tenne, R.; Bar-Sadan, M.; Seifert, G. *J. Phys. Chem. C* **2011**, *115*, 24586–24591.
- (14) Calandra, M. *Phys. Rev. B: Condens. Matter Mater. Phys.* **2013**, *88*, 245428.
- (15) Lin, J.; Cretu, O.; Zhou, W.; Suenaga, K.; Prasai, D.; Bolotin, K. I.; Cuong, N. T.; Otani, M.; Okada, S.; Lupini, A. R.; Idrobo, J.-C.; Caudel, D.; Burger, A.; Ghimire, N. J.; Yan, J.; Mandrus, D. G.; Pennycook, S. J.; Pantelides, S. T. *Nat. Nanotechnol.* **2014**, *9*, 436–442.
- (16) de la Figuera, J.; González, M. A.; García-Martínez, R.; Rojo, J. M.; Hernán, O. S.; Vázquez de Parga, A. L.; Miranda, R. *Phys. Rev. B: Condens. Matter Mater. Phys.* **1998**, *58*, 1169–1172.
- (17) Hammer, R.; Sander, A.; Förster, S.; Kiel, M.; Meinel, K.; Widdra, W. *Phys. Rev. B: Condens. Matter Mater. Phys.* **2014**, *90*, 035446.
- (18) Binnig, O. K.; Rohrer, H.; Gerber, C.; Stoll, E. *Surf. Sci.* **1984**, *144*, 321–335.
- (19) Gibbs, D.; Ocko, B. M.; Zehner, D. M.; Mochrie, S. G. J. *Phys. Rev. B: Condens. Matter Mater. Phys.* **1990**, *42*, 7330–7344.
- (20) Chen, H.; Yang, J.; Rusak, E.; Straubel, J.; Guo, R.; Myint, Y. W.; Pei, J.; Decker, M.; Staude, I.; Rockstuhl, C.; Lu, Y.; Kivshar, Y. S.; Neshev, D. *Sci. Rep.* **2016**, *6*, 22296.
- (21) Sørensen, S. G.; Füchtbauer, H. G.; Tuxen, A. K.; Walton, A. S.; Lauritsen, J. V. *ACS Nano* **2014**, *8*, 6788–6796.
- (22) Liu, H.; Jiao, L.; Yang, F.; Cai, Y.; Wu, X.; Ho, W.; Gao, C.; Jia, J.; Wang, N.; Fan, H.; Yao, W.; Xie, M. *Phys. Rev. Lett.* **2014**, *113*, 066105.
- (23) Xu, H.; Liu, S.; Ding, Z.; Tan, S. J. R.; Yam, K. M.; Bao, Y.; Nai, C. T.; Ng, M.-F.; Lu, J.; Zhang, C.; Loh, K. P. *Nat. Commun.* **2016**, *7*, 12904.
- (24) Helveg, S.; Lauritsen, J. V.; Lægsgaard, E.; Stensgaard, I.; Nørskov, J. K.; Clausen, B. S.; Topsøe, H.; Besenbacher, F. *Phys. Rev. Lett.* **2000**, *84*, 951–954.
- (25) Lauritsen, J. V.; Kibsgaard, J.; Helveg, S.; Topsøe, H.; Clausen, B. S.; Laegsgaard, E.; Besenbacher, F. *Nat. Nanotechnol.* **2007**, *2*, 53–58.
- (26) Bollinger, M. V.; Lauritsen, J. V.; Jacobsen, K. W.; Nørskov, J. K.; Helveg, S.; Besenbacher, F. *Phys. Rev. Lett.* **2001**, *87*, 196803.
- (27) Koshino, M.; Moon, P.; Son, Y.-W. *Phys. Rev. B: Condens. Matter Mater. Phys.* **2015**, *91*, 035405.
- (28) Bonnet, R.; Lherbier, A.; Barraud, C.; Rocca, M. L. D.; Lafarge, P.; Charlier, J.-C. *Sci. Rep.* **2016**, *6*, 19701.
- (29) Liu, K.; Jin, C.; Hong, X.; Kim, J.; Zettl, A.; Wang, E.; Wang, F. *Nat. Phys.* **2014**, *10*, 737–742.
- (30) Lucking, M. C.; Bang, J.; Terrones, H.; Sun, Y.-Y.; Zhang, S. *Chem. Mater.* **2015**, *27*, 3326–3331.